doi: 10.82124/CEAS-GNC-2026-037 CEAS-GNC-2026-037

EuroGNC
Madrid, Spain May 5th-7th 2026

Fast and Accurate Relative Orbit Determination via Angles-Only Batch Unscented Filtering

Alessandro Scalvini PhD Candidate, COMPASS Lab (Politecnico di Milano) Milano, Italy.
alessandro.scalvini@polimi.it

Giacomo Borelli Assistant Professor, COMPASS Lab (Politecnico di Milano) Milano, Italy.
giacomo.borelli@polimi.it

Gabriella Gaias Associate Professor, COMPASS Lab (Politecnico di Milano) Milano, Italy.
gabriella.gaias@polimi.it

ABSTRACT

Autonomous rendezvous and proximity operations are becoming increasingly important in modern space missions, such as formation flying, satellite servicing and active debris removal. These missions often deal with uncooperative targets and must estimate relative motion using only measurements collected by the observer. To lower mission costs and simplify navigation hardware, angles-only (AO) navigation is a promising solution since it relies on cheap, compact, power-efficient and widely available vision-based sensors. However, AO estimation is particularly challenging due to weak observability of the inter-satellite range, requiring more advanced estimation techniques. Batch methods typically yield the most accurate and robust estimates, as they exploit long measurement histories for relative orbit determination (ROD). Traditionally confined to the ground segment due to their high computational cost, recent studies propose the development of lightweight space-borne implementations to complement sequential methods. These filters would use analytical propagation to reduce computation, operate with limited measurements to minimise memory demands, and run as low-priority tasks. Their role is to back up sequential filters in case of divergence and to periodically reinitialise them, preventing stagnation. This paper proposes a novel batch filter based on the unscented transform (UT) for performing ROD within the AO framework. The batch unscented filter (BUF) is an extensively modified version of the non-recursive unscented filter, originally developed to estimate absolute orbits from ground-based range, azimuth, and elevation measurements. Key improvements include an augmented state incorporating both the relative orbital elements and the observer semi-major axis, Monte Carlo-based tuning of the UT, employment of physically meaningful convergence test and a covariance computation procedure inspired by the unscented Kalman filter. The BUF is evaluated in low Earth orbit scenarios inspired by the AVANTI and ARGON experiments, including cases with significant differential drag. Results show that the BUF is capable of estimating the augmented state with accuracy and robustness to noise. The filter remains effective even when using a minimal number of measurements (four) collected over a single orbital period. When combined with analytical propagation, this demonstrates potential for onboard implementation with limited memory and computational resources.

Keywords: Relative Orbit Determination, Angles-Only Navigation, Unscented Transform, Batch Non-Linear Filtering

1 Introduction

Autonomous rendezvous and proximity operations are increasingly relevant for modern space missions, including formation flying [1, 2], satellite servicing [3–5], and active debris removal [3, 6, 7]. In this context, angles-Only (AO) navigation is particularly attractive for far- to mid-range rendezvous with non-cooperative targets. In fact, vision-based sensors (VBS) offer low size, weight and power due to their compact form factor and passive sensing nature. Moreover, they are often already available onboard (e.g., star trackers). However, these benefits come at the cost of weak observability of the inter-satellite range [8, 9], requiring more complex filter architectures [10].

Sequential filters have been traditionally employed for onboard AO state estimation [11]. An extended Kalman filter (EKF) was developed for the AVANTI experiment [10], estimating the relative orbital elements (ROE) of BEESAT-4 relative to BIROS. However, this filter required accurate ground-based initialisation to avoid divergence [12]. Moreover, filter robustness was challenged by complex illumination conditions and intense and time-varying differential drag. Later analyses conducted by Sullivan [13] showed that, even in simulation, the EKF tends to slowly diverge due to weak observability coupled with linearisation errors. To overcome these weakness, Sullivan et al. [14] proposed an unscented Kalman filter (UKF), which improves robustness by bypassing the linearisation step and leveraging the improved state and uncertainty propagation of the unscented transform (UT). The UKF was recently validated in-flight during the StarFoX experiment [15, 16].

Despite these remarkable results [16, 17], divergence risk persists since even few outliers can destabilise sequential filters in weakly observable scenarios. Robustness issues are exacerbated when only few (10-20) measurements per orbit are available. Batch processing offers a promising complementary solution. When implemented onboard, batch methods can serve multiple scopes: (1) validate sequential filters in near real-time; (2) provide reinitialisation upon divergence; (3) periodically re-initialise sequential estimates to prevent stagnation; (4) help the image-processing detect and filter-out potential outliers [17].

Regardless of whether the computation is carried out onboard a spacecraft or on-ground, the most common batch orbit determination (OD) approach relies on non-linear least-squares (LSQ) algorithms [18]. The batch LSQ framework utilises linearised dynamics and linearised measurement and iteratively minimise measurement residuals over a finite (potentially long) time span. This method has proven effective for relative orbit determination (ROD) [19, 20] and was successfully used to post-process ARGON and AVANTI data [17, 21].

Despite the proven performance of the batch iterative LSQ method, it is not fail-safe under highly non-linear dynamics with limited observability. In fact, it may converge to incorrect local minima, diverge from poor initial guesses [17], or suffer from ill-conditioned normal equations [19, 21, 22]. Additionally, the LSQ tends to require a sizeable number of measurements that is uniformly distributed along the relative trajectory [22].

Park et al. [23] addressed some of the challenges of the batch LSQ within the context of *absolute* OD by introducing a non-recursive batch filter based on the UT instead of linearisation. Their method processes ground-based tracking data (range, azimuth, elevation) and demonstrated superior robustness under challenging conditions of large errors and sparse and noisy data).

In this paper, we reformulate the batch unscented filter (BUF) from [23] for angles-only relative orbit determination, with focus on space-borne applicability. The adaptation employs the ROE parametrisation [13] and introduces several modifications. To the best of the authors' knowledge, this algorithm has never been applied to angles-only ROD. This constitutes the main novelty, together with the following updates:

- Implementation of an *analytical* propagation model within the BUF framework, based on Gaias et al. [24]. Unlike the original BUF [23], which relied on numerical integration, this analytical formulation accounts for perturbations from the zonal harmonics J_2, J_4, and J_6, as well as second-order effects from Keplerian motion and J_2, while substantially reducing computational cost, consistent with the findings in [22].

- Adoption of the *fully non-linear* pipeline [25] from the observer orbital elements ($\boldsymbol{\alpha}_O$) and the ROE state ($\delta\boldsymbol{\alpha}$) to azimuth and elevation angles (α, ϵ). This exact transformation provides the highest fidelity and, as shown in [22], it significantly enhances observability.
- Extension of the algorithm capabilities to estimate an augmented state composed by the ROE and other parameters such as the absolute orbit of observer spacecraft, following the analysis conducted by Koenig et al. [26].
- Enhancement of estimation reliability by enforcing physically meaningful convergence conditions on the ROE variations between successive iterations, as suggested in [26].
- Improvement of estimation accuracy by tuning the UT parameters to closely match the covariance resulting from a Monte Carlo simulation, as explained in [13].
- Incorporation of a covariance update step, absent in the original algorithm [23]. The covariance is propagated and updated using a UKF-like strategy, positive definiteness is enforced by zeroing off-diagonal terms and taking the absolute values of the diagonal entries. Finally, covariance inflation is applied after convergence to ensure realistic uncertainty quantification.

These modifications contribute differently to overall performance: the analytical model primarily improves computational efficiency; the augmented state and UT tuning enhance estimation accuracy; and the novel covariance update enables practical uncertainty quantification.

The BUF is evaluated in low-Earth orbit (LEO) scenarios inspired by the AVANTI experiment, including cases with significant differential drag. Results demonstrate accurate and robust estimation even with minimal measurements (four pairs) collected over a single orbital period, suggesting strong potential for onboard implementation.

The remainder of this paper is structured as follows. Section 2 introduces the theoretical background of propagation and measurements models Section 3 describe the batch unscented filter algorithm. In Section 4, the testing methodology and the simulation results are presented and discussed for a representative near-circular LEO scenarios. Finally, Section 5 summarises the key findings of the study and presents the concluding remarks.

2 Mathematical Background

2.1 Dynamics Model

The quasi-non-singular Relative Orbital Elements (ROE) are a convenient parametrisation of the relative motion since they are formulated as a non-linear combination of the absolute orbital elements of the target and observer [13]. In the convention adopted for this work they express the motion of the target relative to the observer. In particular, by considering the vector of classical orbital elements $\boldsymbol{\alpha} = [a, e, i, \Omega, \omega, M]^\top$ and by denoting with $u = \omega + M$ the mean argument of latitude, the dimensional quasi-non-singular ROE $\delta\boldsymbol{\alpha} = a_O\left(\delta a, \delta\lambda, \delta e_x, \delta e_y, \delta i_x, \delta i_y,\right)$, defined for instance in [10]. The components of the state are: the relative semi-major axis $a\delta a$, the relative longitude $a\delta\lambda$, the relative eccentricity vector $a\delta\mathbf{e} = [a\delta e_x, a\delta e_y]^\top$ and the relative inclination vector $a\delta\mathbf{i} = [a\delta i_x, a\delta i_y]^\top$. Where present, the subscript "O" and "T" indicate that the quantities are referred to the observer and target spacecraft, respectively. Importantly, ROE-based representation provides an intuitive and geometrically meaningful representation of relative motion. Consider the Radial-Transversal-Normal (RTN) frame centred on the observer spacecraft. This local coordinate system has the Radial axis ($\hat{\mathbf{R}}$) pointing from the central body toward the observer, the Normal axis ($\hat{\mathbf{N}}$) aligned with the orbital angular momentum and the Transversal ($\hat{\mathbf{T}}$) axis lying in the orbital plane completing the right-handed triad. For a near-circular orbit, the geometric interpretation of the ROE can be easily understood by projecting the relative motion onto the TR-plane and NT-plane, as depicted in Fig. 4.10 of Sullivan. [13]. The selected representation is beneficial in many other ways as it simplifies the enforcement of passive safety using simple geometrical considerations [1], it partitions the ROE state in the weakly observable range-analogue $a\delta\lambda$ from the remaining strongly observable components [19] and it allows to straightforwardly introduce perturbative forces leveraging the Gauss variational equations to obtain efficient analytical propagation schemes [27]. Scalvini et al. [22] demonstrated that the GCL model [24] maintains high accuracy for at least ten observer (chief) orbital periods, and is therefore adopted in this work. This model is valid for arbitrary eccentricity of the observer and accounts for the perturbing effects due J_2, J_4 and J_6 zonal coefficient and for the second order effects due to the Keplerian dynamics and J_2. Gaias et al. [19] demonstrated that accurately modelling perturbative effects (even if partially) is critical to improve the observability of the range-analogue $a\delta\lambda$. Notice however, that in the current implementation the analytical model is *not* taking into the effects of differential drag (DD), which thus remains an unknown perturbation, which can negatively affect the estimation accuracy. Hence, this serves as a proof of filter robustness despite un-modelled relevant relative perturbations. The GCL model propagates both the *mean* relative orbital elements $a\delta\boldsymbol{\alpha}$ and the observer *mean* absolute orbital elements $\boldsymbol{\alpha}_O$ and thus the *analytical* propagation model can be written concisely in a functional form as:

$$\left[a\delta\boldsymbol{\alpha}^\top(t), \boldsymbol{\alpha}^\top(t)\right]^\top \leftarrow \mathbf{F}_{\text{GCL}}(t_0, t, a\delta\boldsymbol{\alpha}(t_0), \boldsymbol{\alpha}(t_0)), \tag{1}$$

where t is the time instant of propagation and t_0 is the initial time instant about which the analytical model is derived. The analytical model $\mathbf{F}_{\text{GCL}}$ will be invoked by the BUF filter to perform a propagation step. It should be noted that the effects of manoeuvres are not analysed in this work. However, the concepts described herein can readily be extended to scenarios involving active propulsion by generalizing the propagation model to incorporate the effects of thruster burns, as discussed, for instance, in [22].

2.2 Measurement Model

In angles-only applications, the observer has very limited information about the relative motion of the target. In particular, at any given time instant the observer perceives the target as a pair of bearing-angles in the VBS frame. In this paper we adopt the bearing-angles convention of [13], which defines the pair of azimuth α and elevation ϵ. Thus, we express the vector of modelled measurements as:

$$\mathbf{y}(t) = \begin{pmatrix} \alpha(t) \\ \epsilon(t) \end{pmatrix} = \begin{pmatrix} \arcsin\left({}^{\text{VBS}}\delta y(t)/||{}^{\text{VBS}}\delta\mathbf{r}(t)||_2\right) \\ \arccos\left({}^{\text{VBS}}\delta x(t)/{}^{\text{VBS}}\delta z(t)\right) \end{pmatrix}, \tag{2}$$

where ${}^{\text{VBS}}||\delta\mathbf{r}(t)||_2 = \left[{}^{\text{VBS}}\delta x(t), {}^{\text{VBS}}\delta y(t), {}^{\text{VBS}}\delta z(t)\right]^\top$ is the vector of the Cartesian relative position of the target relative to the observer, expressed in VBS coordinates at the generic time instant t. Assume now that the VBS sensor is oriented in the anti-flight direction, meaning that the VBS bore-sight (z-axis) points in the opposite direction of $\hat{\mathbf{T}}$, the x-axis of the VBS points in the direction of $\hat{\mathbf{R}}$ and the y-axis of the VBS points in the direction of $\hat{\mathbf{N}}$ of the RTN frame described in Section 2.1.

Recalling now that the information available to the observer spacecraft at a generic time instant t include: (i) the current knowledge of the *mean* ROE, (ii) the current knowledge of the *mean* absolute OE of the observer and (iii) the knowledge of the orientation of the VBS frame with respect to the Earth centred inertial (ECI) frame. The first is obtained from the filter estimate, propagated to t, the second usually comes from external measurements (e.g., GNSS), also propagated to t. In this work, the propagation is performed using the GCL model of Eq. (1). The third comes from the VBS sensor itself. In fact, the VBS usually is a star-tracker, thus, it automatically provides its absolute attitude as well (in the far-range). To compute the bearing angles using Eq. (2), the Cartesian position in the VBS frame $\delta\mathbf{r}(t)$ must be computed from the available information. In this work we use the non-linear transformation described in [25]. The complete pipeline is detailed in [24, 25] and is not reported here for the sake of conciseness. However, we recall here the main steps: (i) retrieving the *mean* absolute orbital elements of the target $\boldsymbol{\alpha}_T$ from the definition of the ROE. (ii) applying a mean-to-osculating transformation to obtain the *osculating* counterparts of $\boldsymbol{\alpha}_O$ and $\boldsymbol{\alpha}_T$. In this work the second order transformation adopted also in [25] is employed. Notice that this transformation is critical to obtain reasonable observability [13]. (iii) Converting the osculating Keplerian elements to the equivalent Cartesian state (expressed in ECI) using a Keplerian-to-Cartesian transformation [18]. (iv) computing the inertial relative position by subtracting the relative position of the observer from the one of the target. (v) Applying the rotation rotation matrix ${}^{\mathrm{VBS}}\mathbf{R}_{\mathrm{ECI}}(t)$ to express the relative position in the VBS frame ${}^{\mathrm{VBS}}\delta\mathbf{r}(t)$. The matrix is obtained from the absolute attitude of the VBS and is available from the VBS (star-tracker) itself.

The steps of the non-linear transformation described above and followed by the application of Eq. (2) can be packaged into a single function $\mathbf{h}_{\mathrm{NL}}$. This constitutes our measurement model which converts the current knowledge of the *mean* ROE and *mean* absolute OE of the observer to the modelled bearing-angles:

$$\mathbf{y}(t) \leftarrow \mathbf{h}_{\mathrm{NL}}(a\delta\boldsymbol{\alpha}(t), \boldsymbol{\alpha}_O(t), {}^{\mathrm{VBS}}\mathbf{R}_{\mathrm{ECI}}(t)). \tag{3}$$

3 The Batch Unscented Filter

This section presents the batch unscented filter (BUF), a modification of the non-recursive unscented batch filter originally proposed by Park et al. [23], specifically adapted to address the weakly observable problem of angles-only relative orbit determination. First, we define the full state $\mathbf{x}_{\mathrm{full}}$, obtained by stacking the *mean* ROE and the observer *mean* absolute OE:

$$\mathbf{x}_{\mathrm{full}}(t_{\mathrm{est}}) = \begin{bmatrix} a\delta\boldsymbol{\alpha}(t_{\mathrm{est}}) \\ \boldsymbol{\alpha}_O(t_{\mathrm{est}}) \end{bmatrix} \tag{4}$$

Note that the state is expressed at the estimation time $t = t_{\mathrm{est}}$, *i.e.*, the instant at which the state is to be estimated. We could also augment $\mathbf{x}_{\mathrm{full}}$ with additional parameters (e.g., drag terms, empirical accelerations, VBS bias, etc.). When parameters are also included, the propagation model (Eq. (1)) has to be modified to also account for the time propagation of their dynamics. However, these are not included in this work and are left for future analysis. The full state of Eq. (4) can thus be partitioned as:

$$\mathbf{x}_{\mathrm{full}}(t_{\mathrm{est}}) = \begin{bmatrix} \mathbf{x}_{\mathrm{est}}(t_{\mathrm{est}}) \\ \mathbf{x}_{\mathrm{fixed}}(t_{\mathrm{est}}) \end{bmatrix}. \tag{5}$$

The first portion (subscript "est") collects the elements of $\mathbf{x}_{\mathrm{full}}(t_{\mathrm{est}})$ that we want to estimate, while the second (subscript "fixed") contains those elements simply propagated in time but not refined by the estimation procedure. In the context of this article, we have:

$$\mathbf{x}_{\mathrm{est}}(t_0) = \left[a\delta\boldsymbol{\alpha}(t_0)^\top, a_O(t_0)\right]^\top, \tag{6}$$

$$\mathbf{x}_{\mathrm{fixed}}(t_0) = \left[e_O(t_0), i_O(t_0), \Omega_O(t_0), \omega_O(t_0), M_O(t_0)\right]^\top. \tag{7}$$

Thus, the estimated state is composed by the ROE augmented by the observer semimajor axis. This is done since the analysis of Koenig et al. [26] demonstrated that a_O is strongly observable even in an AO scenario. We explicitly indicated that the quantities are estimated at the initial time $t_{\mathrm{est}} = t_0$, as typically done in problems of (relative) orbit determination. In order to initialise the algorithm we also need an initial estimate of the uncertainty of $\mathbf{x}_{\mathrm{est}}$ in the form of a covariance matrix $\mathbf{P}_{\mathrm{est}}$, whose dimensions and entries are coherent with those of $\mathbf{x}_{\mathrm{est}}$. The tuple $(\mathbf{x}_{\mathrm{est}}, \mathbf{P}_{\mathrm{est}})$ is progressively updated by the BUF iterative procedure, as shown in the in Algorithm 1 and described in the following.

Algorithm 1 Batch Unscented Filter (BUF) Algorithm

```
function BUF ($t_{\text{est}}$, $\mathbf{x}_{\text{full}}(t_{\text{est}})$, $\mathbf{P}_{\text{est}}$, $\mathbf{j}_{\text{est}}$, $\{t_{\text{meas}}\}$, $\{\mathbf{z}_{\text{meas}}(t)\}$, $\left\{{}^{\text{VBS}}\mathbf{R}_{\text{ECI}}(t)\right\}$, $\mathbf{R}_{\text{noise}}$, $\sigma$, $\kappa$, $\beta$)
    $j \leftarrow 0$
    while $|\Delta a\delta a| >= \Delta a\delta a_{\min}$ & $|\Delta a\delta\boldsymbol{\alpha}| >= \Delta a\delta\boldsymbol{\alpha}_{\min}$ & $j < j_{\max}$ do
        $j \leftarrow j + 1$
        $\boldsymbol{\mathcal{X}}(t_{\text{est}}), \bar{\bar{\mathbf{x}}}_{\text{full}}(t_{\text{est}}), \bar{\bar{\mathbf{P}}}_{\text{est}} \leftarrow$ SIGMAPOINTS ($\mathbf{x}_{\text{full}}(t_{\text{est}})$, $\mathbf{P}_{\text{est}}(t_{\text{est}})$, $\mathbf{j}_{\text{est}}$, $\sigma$, $\kappa$))
        $\{\boldsymbol{\mathcal{X}}(t)\} \leftarrow \mathbf{F}_{\text{GCL}}\left(t_{\text{est}}, \{t_{\text{meas}}\}, \boldsymbol{\mathcal{X}}(t_{\text{est}})^{[:,\,1:6]}, \boldsymbol{\mathcal{X}}(t_{\text{est}})^{[:,\,7:12]}\right)$
        $\{\boldsymbol{\mathcal{Y}}(t)\} \leftarrow \mathbf{h}_{\text{NL}}\left(\{\boldsymbol{\mathcal{X}}(t)\}^{[:,\,1:6,\,:]}, \{\boldsymbol{\mathcal{X}}(t)\}^{[:,\,7:12,\,:]}, \left\{{}^{\text{VBS}}\mathbf{R}_{\text{ECI}}(t)\right\}\right)$
        $\left\{\bar{\bar{\mathbf{y}}}(t)\right\} \leftarrow \sum_{l=0}^{2n_{\text{est}}} w_l^{(m)} \{\boldsymbol{\mathcal{Y}}(t)\}^{[:,\,l]}$
        $\mathbf{P}^{\mathbf{y}} \leftarrow \sum_{l=0}^{2n_{\text{est}}} w_l^{(c)} \left(\{\boldsymbol{\mathcal{Y}}(t)\}^{[:,\,l,\,:]} - \left\{\bar{\bar{\mathbf{y}}}(t)\right\}\right)\left(\{\boldsymbol{\mathcal{Y}}(t)\}^{[:,\,l,\,:]} - \left\{\bar{\bar{\mathbf{y}}}(t)\right\}\right)^{\top}$
        $\mathbf{P}^{\mathbf{xy}} \leftarrow \sum_{l=0}^{2n_{\text{est}}} w_l^{(c)} \left(\boldsymbol{\mathcal{X}}(t)^{[:,\,l]} - \bar{\bar{\mathbf{x}}}(t)\right)\left(\{\boldsymbol{\mathcal{Y}}(t)\}^{[:,\,l]} - \left\{\bar{\bar{\mathbf{y}}}(t)\right\}\right)^{\top}$
        $\mathbf{K} = \mathbf{P}^{\mathbf{xy}}\left(\mathbf{P}^{\mathbf{y}}\right)^{-1}$
        $\{\boldsymbol{\rho}(t)\} \leftarrow \{\mathbf{z}_{\text{meas}}(t)\} - \left\{\bar{\bar{\mathbf{y}}}(t)\right\}$
        $\Delta\mathbf{x}_{\text{full}}(t_{\text{est}}) = \mathbf{K}\{\boldsymbol{\rho}(t)\}$
        $|\Delta a\delta a| \leftarrow |\Delta\mathbf{x}_{\text{full}}^{[1]}(t_{\text{est}})|$, $|\Delta a\delta\boldsymbol{\alpha}| \leftarrow |\Delta\mathbf{x}_{\text{full}}^{[1:6]}(t_{\text{est}})|$
        $\mathbf{x}_{\text{full}}(t_{\text{est}}) \leftarrow \bar{\bar{\mathbf{x}}}_{\text{full}}(t_{\text{est}}) + \Delta\mathbf{x}_{\text{full}}(t_{\text{est}})$
        $\mathbf{P}_{\text{est}} \leftarrow \bar{\bar{\mathbf{P}}}_{\text{est}} - \mathbf{K}\,\mathbf{P}^{\mathbf{xy}}\,(\mathbf{K})^{\top}$
        $\mathbf{P}_{\text{est}} \leftarrow$ DIAG (|DIAG ($\mathbf{P}_{\text{est}}$)|)
    end while
    $\mathbf{P}_{\text{est}} \leftarrow 9\mathbf{P}_{\text{est}}$
return $\mathbf{x}_{\text{full}}(t_{\text{est}})$, $\mathbf{P}_{\text{est}}$
end function
```

The BUF takes the following inputs:

- t_{est}: the estimation time,
- $\mathbf{x}_{\text{full}}$: the current knowledge of the full vector at t_{est}. This contains the initial guess of x_{est}.
- $\mathbf{P}_{\text{est}}$: covariance associated to the initial guess of of x_{est} (see line 16). Differently from the original paper, the BUF is capable of updating also this quantity.
- $\mathbf{j}_{\text{est}}$: vector of indices that indicates which elements of $\mathbf{x}_{\text{full}}$ compose x_{est}.
- $\{t_{\text{meas}}\}$: time series of time instants at which the measurements are received.
- $\{\mathbf{z}_{\text{meas}}(t)\}$: time series of measurements (pairs of azimuth and elevation) measured by the VBS sensor at the time instants in $\{t_{\text{meas}}\}$.
- $\left\{{}^{\text{VBS}}\mathbf{R}_{\text{ECI}}(t)\right\}$: time series of rotation matrices obtained from the VBS sensor operating as star-tracker at the time instants in $\{t_{\text{meas}}\}$. Notice that the attitude information is assumed synchronous with the bearing-angles measurements.
- $\mathbf{R}_{\text{noise}}$: sensor noise matrix affecting the VBS. Assumed constant in time.
- σ, κ, β: UT tunable parameters according to the notation used in [13].

Throughout this work, the quantities enclosed in curly brackets ("$\{\square\}$") represent time series. The temporal dimension is consistently assigned to the third index. Hence, a time series of 2×2 matrices is expressed as a three-dimensional array of size $2 \times 2 \times n_{\text{instants}}$.

The algorithm starts by generating an array of $2n_{\text{est}} + 1$ sigma points, where n_{est} is simply the size of $\mathbf{x}_{\text{est}}$. These sigma points are column-vectors that are collected in the array $\mathcal{X}(t_{\text{est}})$. The array is two-dimensional, having on each column one sigma point. All the sigma points are at the same time instant t_{est}. The pseudocode of the function used for this task is reported in Algorithm 2 for completeness.

Algorithm 2 Sigma Points Generation

```
function sigmaPoints($\mathbf{x}_{\text{full}}(t)$, $\mathbf{P}_{\text{var}}(t)$, $\mathbf{j}_{\text{var}}$, $\sigma$, $\kappa$ )
    $\ell_{\text{var}} \leftarrow$ length($\mathbf{j}_{\text{var}}$)
    $\gamma = \sigma^2(\ell_{\text{var}} + \kappa) - \ell_{\text{var}}, \quad \zeta \leftarrow \sqrt{\ell_{\text{var}} + \gamma}$
    $\mathcal{X}(t) \leftarrow$ repeatMatrix($\mathbf{x}_{\text{full}}(t),\ 1,\ 2\ell_{\text{var}} + 1$)
    $\mathcal{X}^{[\mathbf{j}_{\text{var}},:]}(t) \leftarrow \mathcal{X}^{[\mathbf{j}_{\text{var}},:]}(t) + \left(\mathbf{0}, \zeta\sqrt{\mathbf{P}_{\text{var}}(t)}, -\zeta\sqrt{\mathbf{P}_{\text{var}}(t)}\right)$
    $\bar{\bar{\mathbf{x}}}_{\text{full}}(t) \leftarrow \sum_{l=0}^{2\ell_{\text{var}}} w_l^{(m)} \mathcal{X}_l(t)$
    $\bar{\bar{\mathbf{P}}}_{\text{var}}(t) \leftarrow \sum_{l=0}^{2\ell_{\text{var}}} w_l^{(c)} \left(\mathcal{X}(t)^{[:,\,l]} - \bar{\bar{\mathbf{x}}}(t)\right)\left(\mathcal{X}(t)^{[:,\,l]} - \bar{\bar{\mathbf{x}}}(t)\right)^\top$
    return $\bar{\bar{\mathbf{x}}}_{\text{full}}(t)$, $\bar{\bar{\mathbf{P}}}_{\text{var}}(t)$
end function
```

Notice that this function applies the UT only to the elements of $\mathbf{x}_{\text{full}}$ indicated by the vector $\mathbf{j}_{\text{var}}$, the other components are left constant and appear unvaried in each sigma point. The sigmaPoints function accepts also the process noise matrix as input ($\mathbf{Q}_{\text{noise}}$) but in this work it is set to zero for simplicity.

Finally, consider that the weights can be pre-computed for both Algorithms using the following [13]:

$$w_l^{(m)} = \begin{cases} \dfrac{\gamma}{\ell_{\text{var}} + \gamma} & \text{for } l = 0 \\ \dfrac{1}{2(\ell_{\text{var}} + \gamma)} & \text{for } l = 1, \ldots, 2\ell_{\text{var}} \end{cases}$$

$$w_l^{(c)} = \begin{cases} \dfrac{\gamma}{\ell_{\text{var}} + \gamma} + (1 - \sigma^2 + \beta) & \text{for } l = 0 \\ \dfrac{1}{2(\ell_{\text{var}} + \gamma)} & \text{for } l = 1, \ldots, 2\ell_{\text{var}}. \end{cases}$$

Besides the array of sigma points, the function updates also the mean and covariance of $\mathbf{x}_{\text{est}}$ and returns the predicted full vector $\bar{\bar{\mathbf{x}}}_{\text{full}}$ and predicted covariance $\bar{\bar{\mathbf{P}}}_{\text{est}}$ of $\bar{\bar{\mathbf{x}}}_{\text{est}}$. The second step is to propagate each sigma point to each time instant in $\{t_{\text{meas}}\}$. This is done with the propagation model $\mathbf{F}_{\text{GCL}}$ described in Section 2.1. Assuming that the propagation function is properly vectorised, we pass to the function all the sigma points and all the time instants together. Notice that the superscript "$[i,\ j,\ k]$" indicates the indexing performed on the array to extract the necessary components. The output of the propagation will be three-dimensional, since it corresponds to a time series of an array of propagated sigma points $\boldsymbol{\mathcal{X}}(t_i)$ propagated to each of the time instants in $\{t_{\text{meas}}\}$. Consequently, its dimensions will be: $[n_{\text{full}}, 2n_{\text{est}} + 1, n_{\text{meas}}]$. The quantity n_{meas} is simply the number of time instants in $\{t_{\text{meas}}\}$. The time-series $\{\boldsymbol{\mathcal{X}}(t)\}$ is then passed to the measurement model $\mathbf{h}_{\text{NL}}$ that transforms each of the $2n_{\text{est}} + 1 \times n_{\text{meas}}$ propagated sigma points in the corresponding pair of azimuth and elevation. These are stored in a second time series of measurements sigma points $\{\boldsymbol{\mathcal{Y}}(t)\}$ whose columns correspond to the (α, ϵ) pairs and each matrix in the third dimension correspond again to a time instant in $\{t_{\text{meas}}\}$. The dimensions of this array are: $[2, 2n_{\text{est}} + 1, n_{\text{meas}}]$. The following step computes the time series of the UT-weighted expected values $\left\{\bar{\bar{\mathbf{y}}}(t)\right\}$ by applying the weighted sum along the second dimension. A similar procedure is applied to obtain the covariance of the times series of predicted measurements $\mathbf{P}^{\mathbf{y}}$ and the cross-correlation of the state at estimation time with the times series of the predicted measurements $\mathbf{P}^{\mathbf{xy}}$. From those two quantities a Kalman-like gain matrix $\mathbf{K}$ is readily obtained [23]. Subsequently, the residual vector time series is computed by subtracting the (time series of the) predicted expected value from the (time series of) the measured bearing angles. Then, the state update is computed and the convergence test-variables are updated. The state estimate and the associated covariance are updated following a measurements update analogous to the one used by the UKF, but which now accounts for all the time history of the residuals. Thus, state estimate and covariance are now correlated to the whole time history of measurements, instead of only the single current values as in the UKF. Convergence is achieved when the **while** loop (see line 3) is exited, either because the minimum tolerance on the increment has been reached or the maximum number of iterations has been exceeded. After convergence, the covariance is inflated by a factor of 9 (corresponding to the 3σ confidence level), as empirical evidence indicates that the BUF tends to be overconfident in its state uncertainty estimates.

4 Preliminary Testing

4.1 Testing Methodology

Preliminary testing of algorithm is performed in a variety of LEO scenarios typical of far-to mid-range rendezvous. In particular the physical parameters of the observer and target spacecraft are inspired by the AVANTI experiment and reported in Tab. 1. In the most general and challenging case for angles-only observability in low Earth orbit, differential drag is present. Therefore, the filter must demonstrate robust convergence even under such conditions. Since the analytical model described in Section 2.1 and employed by the BUF does not currently account for differential drag, this scenario serves to assess the filter's capability to converge despite model mismatches caused by un-modelled perturbations, which may be significant. Future developments may improve this aspect for low Earth orbit applications. All the simulations are conducted using a high-fidelity simulator whose settings are specified in Tab. 2. The output of the simulation is the ground-truth for the analysis. Notice that the attitude dynamics of spacecraft is not simulated but only emulated. In fact, the orientation of the VBS bore-sight is kept constantly aligned with the anti-flight direction.

Table 1 Spacecraft Physical Parameters

Parameter	**Observer**	**Target**
Mass (kg)	130	1
Area (m^2)	0.5984	0.0100
Drag Coefficient (-)	2.5	2.2
Ballistic Coefficient (kg/m^2)	0.0115	0.0220

Table 2 Ground Truth Simulation Parameters

Parameter	**Value**
Duration	2 observer orbit periods
Step	30 (s)
Integrator	Dormand-Prince 5th order
Geo-potential	GGM03S 30×30
Atmospheric Drag	Cannonball model
Atmospheric Density	NRLMSISE 00
Manoeuvres	None (unforced motion)
VBS bore-sight	Anti-flight direction

To generate the synthetic batch of data used by the BUF filter, the bearing-angles measured by the VBS are corrupted with zero-mean Gaussian noise $\sigma_{\text{VBS}} = 40$ arcsec, similarly to [19]. The orientation of VBS with respect to the ECI, indicated by the rotation matrix ${}^{\text{VBS}}\mathbf{R}_{\text{ECI}}$, is usually provided by the star-trackers on board the observer and for this analysis is assumed to be perfectly known.

Six relevant simulation scenarios are defined by the combining two initial absolute orbits of the observer (LEO1 and LEO2) and three initial relative orbit of the target with respect to the observer (RO1, RO2 and RO3). These are reported in Tab. 3 and in Tab. 4, respectively. The LEO cases are selected to isolate the effects of this perturbation on the estimation. Orbit LEO1 is characterised by negligible differential drag given the high altitude $h = 800$ (km). Orbit LEO2 is instead selected to place the spacecraft at a much lower orbit of $h = 500$ (km), where the DD perturbation is second only to the one produced by J_2 [17]. The relative orbits in Tab. 4 are selected to cover three relevant scenarios: RO1 is a far-range and passively safe relative orbit, typical starting point for a rendezvous. Given the relatively large $a\delta e_x$ and $a\delta i_x$, the orbit is strongly influenced by the zonal perturbation, which increases the observability of the relative motion when accounted for by the filter [19]. The second relative orbit is a modified case of RO1 where a moderate approaching motion due to a non-zero $a\delta a$ is added. This is expected to be a very difficult case to estimate. Finally, RO3 is characterised by a medium-range, in-train formation. Here the effect of zonal perturbation is minimal and so is the observability [26].

Table 3 Initial observer Orbit Test Cases

Case	a_O (km)	e_O (-)	i (deg)	Ω_O (deg)	ω_O (deg)	M_O (deg)
LEO1	7178.1	0.0016	98	20	20	10
LEO2	6878.1	0.0016	98	20	20	10

Table 4 Initial Relative Orbit Test Cases

Case	$a\delta a$ (m)	$a\delta\lambda$ (m)	$a\delta e_x$ (m)	$a\delta e_y$ (m)	$a\delta i_x$ (m)	$a\delta i_y$ (m)
RO1	0	−30000	−400	0	400	0
RO2	−50	−30000	−400	0	400	0
RO3	0	−10000	−20	0	20	0

The objective of the BUF filter is to estimate the ROE parameters and the observer semi-major axis at the initial time $t_{\text{est}} = t_0 = 0$ (s). This does not constitute a loss of generality, since the estimate can then be propagated to any time instant or the filter can be formulated to estimate the augmented state at any time instant. Similarly to a non-linear batch LSQ, the BUF needs an initial guess of the quantities to be estimated and the covariance of such initial guess. Normally, in LEO this *a priori* information is provided via NORAD two-line-elements (TLE). The uncertainty on the observer absolute OE and on the ROE are reported in Tab. 5. These values are a conservative given the accuracy we can reasonably expect from TLE [19]. In particular the uncertainty on $a_O(t_0)$ is set to a considerably large value, representing a worst-case scenario in order to stress test the BUF. The uncertainty on the other components of $\boldsymbol{\alpha}_O(t_0)$ is computed accordingly to [26]. To generate the initial guess, the true initial OE of the observer and the ROE, reported in Tab. 3 and 4, are corrupted with a Gaussian error sampled accordingly to the values in Tab. 5. Finally, the main estimation settings are reported in Tab. 6. Importantly, the filter is given a set of 60 uniformly spaced measurements, corresponding to 30 measurements per orbit. Uniformly spaced measurements are adopted to emulate an operational scenario with regular observation windows, ensuring consistent coverage of the relative orbit geometry throughout the observation arc. As discussed in [22], this should be a reasonably favourable scenario for the observability, since it is equivalent to having a constant visibility of the relative orbit from the perspective of the observer.

Table 5 Uncertainty Settings

Observer OE standard deviation	
$\sigma_{a_O(t_0)}$	$= 1000$ (m)
$\sigma_{[e_O, i_O, \Omega_O, \omega_O, M_O]}$	$= \sigma_{a_O(t_0)}/a_O(t_0)$
ROE standard deviation	
$\sigma_{a\delta\lambda}$	$= 1000$ (m)
$\sigma_{a\delta a,\, a\delta e_x,\, a\delta e_y,\, a\delta i_x,\, a\delta i_y}$	$= 100$ (m)

To push the BUF filter to its operational limits, a second analysis is conducted under substantially more demanding conditions. Specifically, the previous test cases are repeated with two fundamental modifications: the simulation time span is reduced to a single observer orbital period and the filter is supplied with only the theoretical minimum number of measurements (rounded to a multiple of two). Consequently, to estimate the 7 parameters ($a\delta a$, $a\delta\lambda$, $a\delta e_x$, $a\delta e_y$, $a\delta i_x$, $a\delta i_y$, and a_O), the filter is given four azimuth–elevation pairs. In this configuration, the BUF is therefore challenged to achieve relative

Table 6 Filter Settings

Setting	Value
Measurements	60 uniformly spaced (Azimuth, Elevation)
Estimated ROE	$a\delta a$, $a\delta\lambda$, $a\delta e_x$, $a\delta e_y$, $a\delta i_x$, $a\delta i_y$
Estimated observer OE	a_O
Non-estimated observer OE	e_O, i_O, Ω_O, ω_O, M_O
Max Iterations	15
$\Delta\delta a_{\min}$	0.1 (m)
$\Delta a\delta\boldsymbol{\alpha}_{\min}$	0.01 (m)
UT parameters	$\sigma = 0.5, \kappa = 1.0, \beta = 5.0$

orbit determination from just four measurements, thus testing its robustness under very severe constrains which might represent a scenario where extreme data gaps occurred.

4.2 Results: Analysis 1

The results of the relative orbit estimation performed with the BUF for the scenarios introduced in Sec. 4.1 are presented in Figs. 1–2. For conciseness, only the plots corresponding to the most challenging configuration (weakly observable RO3) are shown. Nevertheless, Tabs. 9 and 7 summarize the estimation performance for all six test cases. Each figure is composed by a panel of four plots that help visualise the outcome of the estimation. Starting from the top-left we find a 3D view of three relative orbits, represented in the RTN frame centred in the observer spacecraft, as discussed in Sec. 2.1. The nominal (NOM) relative orbit, depicted in black solid line, is obtained by propagating the *true* initial conditions of Tab. 3 and 4 using the *analytical* model $\mathbf{F}_{\text{GCL}}$. The initial guess (GUESS) relative orbit, depicted in magenta solid line, is instead obtained propagating the state used to initialise the filter. Finally, the post-BUF-estimation (BUF) relative orbit, depicted in blue solid line, is obtained propagating the output of the BUF algorithm after convergence. It is important to highlight that each of these three orbits is propagated with the analytical model of Eq. (1). Thus in all of them, the effects of differential drag remain completely unaccounted for. To understand the direction of motion, the star and end point are portrayed with green and red markers, respectively. Proceeding in a counter-clockwise manner, in the second row of each figure we find the projection of previous plot onto the TN-plane (bottom left plot) and RN-plane (bottom right plot). Finally, moving to the top-right corner, the upper-right plot report an additional 3D view. Here, to the nominal orbit just described, we super-imposed the true (TRUE) relative orbit, depicted in dashed cyan line. The difference between NOM and TRUE orbit is that the the latter is obtained from the high-fidelity simulator and is the actual ground-truth. Notice that the difference between the NOM and TRUE relative orbits is practically negligible in LEO1 scenarios since the differential drag perturbation (not accounted for by the analytical model) is barely present. It is however much more evident in LEO2 cases, given the much lower orbit and intense DD. The distinction between the two is important since the NOM curve can be interpreted as an upper bound on BUF performances. This because the filter tries to fit the measurements using its (faulty) knowledge of the ground-truth. Thus, the more these two are different, the greater the estimation error will be since the filter will compensate the erroneous knowledge of the dynamics by introducing errors in the estimate so as to minimise the residuals. In particular the upper-right plot of Fig. 2 clearly display the difference. The NOM orbit is clearly closed without any drift. Indeed $a\delta a(t_0) = 0$ (m) and no differential drag is modelled. However, the DD is present and relatively strong in the ground-truth simulation, giving rise to an important discrepancy between modelled and ground-truth dynamics. This will certainly reflect in the estimation quality. Finally, the blue diamond markers represent the data-points *i.e.*, the positions on the (TRUE) relative orbit corresponding to the time-instants at which a measurement is taken. Given that we are describing the fist analysis (see Tab. 6), a total of 60 data points are depicted and most of the relative orbit is covered.

Figures 1-2 and Tabs 9-7 show a net improvement of the initial guess (GUESS) is achieved in all scenarios. This is particularly clear when considering the RN-plane projection, where the BUF and NOM curves are almost coincident in both scenarios. By analysing the TN-plane, we can still see that the shape and dimension of the curves improves substantially after the estimation, but the curves still display a separation along the $\hat{\mathbf{T}}$ axis. This separation is mostly due to an imperfect estimate of the range-equivalent in ROE-space, namely the weakly-observable $a\delta\lambda$. The improvement of the estimate is confirmed by looking at the estimation errors reported in Tab. 9. Here we can see that all estimated components (including the observer semimajor axis) improve substantially from the initial guess in all cases, with only very few exception. In fact, only the error on $a\delta\lambda$ and a_O worsens for the RO3 scenarios. As anticipated before, this is the worst case for what concerns observability since the two spacecraft are practically flying in a in-train configuration. Moreover, from the table it is clear that the LEO2-RO3 case is the worst possible. This is again coherent with the expectations, given that it is the least observable coupled with the un-modelled differential drag perturbation. However, even in these harsh cases, the estimate never diverges and all the other parameters are adequately estimated. In the same table we can see the confidence of the estimate, represented by the standard deviation $\sigma(\square)$. Notice that uncertainty level is reasonable in all scenarios except for the two problematic ones, where the uncertainty is suspiciously small. This is useful, since an evidently overconfident estimate (especially on the weakly observable $a\delta\lambda$) might be used as an heuristic test to determine a possible failure of the estimation procedure. In fact, when the filter produces unrealistically small uncertainties on poorly observable states, it suggests possible inconsistencies between the estimated state and the true one. Finally, Tab. 7 complements previous results by reporting the mean and standard deviation of the residuals of the GUESS, BUF and NOM orbits for all scenarios. The mean and standard deviation are computed on the time-history of the residuals as described in [22]. Ardeans [17] explained that these two quantities are good indicators of the estimation quality. In particular, the mean $\bar{\bar{\rho}}_{\square}$ should be as close to zero as possible and the variance $\sigma_{\square}$ should be around the noise level. Moreover the author discussed how biases in the mean values of the residuals indicate that there are dynamical effects not captured by the propagation model used by the filter. However, the author also clarifies that this information is incomplete since an estimator might converge to a wrong local optimum (very small $\bar{\bar{\rho}}_{\square}$ and $\sigma_{\square}$) due to the non-linearities of the dynamics coupled with the weak observability issue. All these observations are proven correct also in our analysis. Indeed, $\bar{\bar{\rho}}_{\square}$ is practically zero in all LEO1 and slightly grows in the LEO2 scenarios, due to the un-modelled DD. This is confirmed also by the NOM mean residual in elevation, which grows substantially from the LEO1 to LEO2 cases. Notice moreover that the lack of observability introduced by RO3 cases acts in a similar manner: indeed, the modelled observability-improving perturbations are here almost absent, leaving only those higher order effects (plus the DD) that are not accounted for by the analytical model. In conclusion, the results of the first analysis show that the filter is capable of greatly improving the initial guess in all the test cases, even in presence of un-modelled and strong DD (LEO2) and/or in case of very limited observability (RO3). Even though some loss of accuracy is experienced in the in-train configuration, which is a worst case scenario for the observability, the BUF always converges to acceptable values. In all other cases, the BUF displays high accuracy level. Regarding computational performance, the BUF converges in approximately 2.38 seconds when processing 60 measurements, as measured on a Dell Latitude 5440 laptop equipped with an Intel Core i7 vPro processor (Intel64 Family 6, Model 186) running at 1.9 GHz. These results confirm the strong robustness of this algorithm and suggest that it may compete with a LSQ approach in terms of accuracy, as claimed in [23].

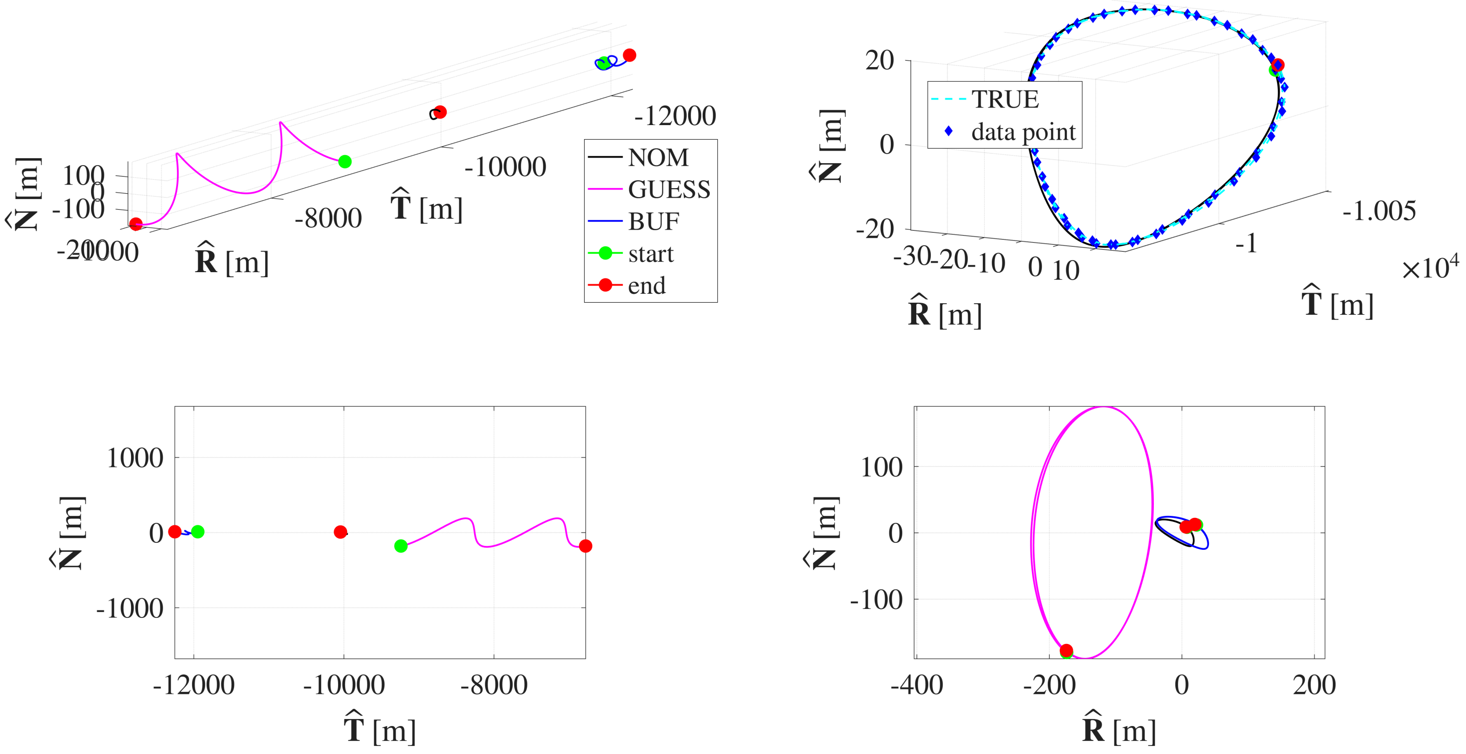

Fig. 1 **Analysis 1 (LEO1 - RO3): Results of the estimation procedure.**

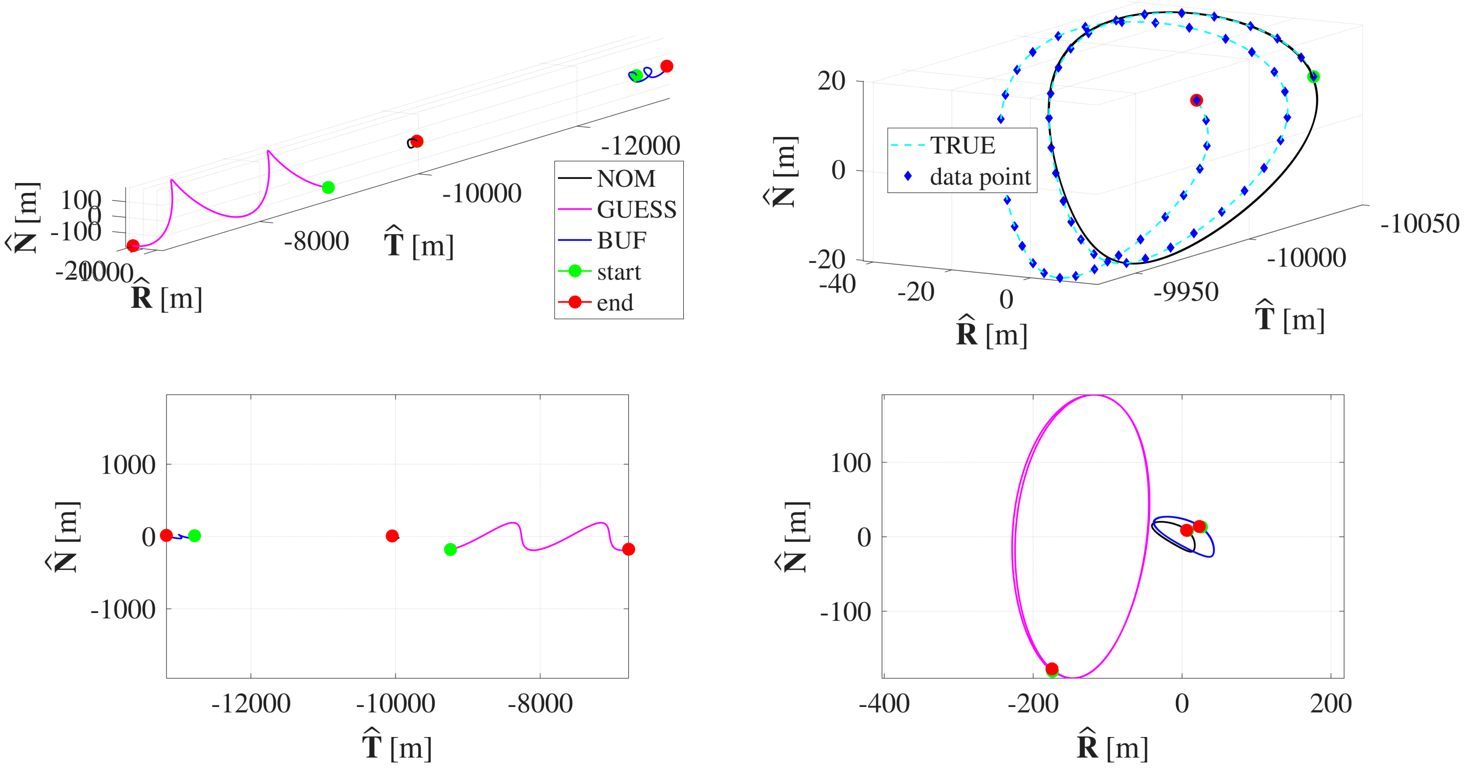

Fig. 2 **Analysis 1 (LEO2 - RO3): Results of the estimation procedure.**

4.3 Results: Analysis 2

It is recalled here that the second analysis uses the same methodology and parameters of the first one with only two important exceptions: the simulation time is halved and the batch of data used by the BUF is composed of only four azimuth–elevation pairs. The results of the relative orbit estimation using the BUF are shown in Figs. 3–4 and complemented by Tabs. 10 and 8. Also in this second analysis we report only the figures corresponding to the cases for Analysis 1. From the figures we can observe a somewhat surprising outcome. One would expect that by reducing substantially the amount of data used by the filter, the estimation accuracy would be negatively affected. Interestingly, not only the BUF is still capable to accurately estimate the parameters, but also produce similar results to previous analysis at a fraction of the computational cost. Even more surprisingly, the greatest improvement is achieved in the hardest scenarios: namely the weakly observable RO3 cases. This appears clear by comparing the scenarios in Fig. 1 and 2 of first analysis with the corresponding results obtained in the second one, displayed in Fig. 3 and 4. In these cases, the improvement is not limited to the strongly observable quantities but also extends to the weakly observable $a\delta\lambda$, which nearly coincides with its true value. However, we cannot yet rule out the possibility that this outcome is partly fortuitous; under different scenarios with similarly poor observability conditions, the results might differ. Once again, the plots are complemented with the estimation error table of each scenario (Tab. 10) and the residuals table (Tab. 8) which confirm the intuition gained from the pictures. The results of this second analysis are extremely encouraging since the BUF might be able to robustly perform ROD using a minimal amount of data collected during a single orbit. This is not only useful for on-ground estimation, but would pave the way to an space-borne implementation, since it would allow minimal computational and memory requirements. A possible explanation of this behaviour is in the numerical conditioning of matrix $\mathbf{P}^{\mathbf{y}}$, introduced in line 9 of Algorithm 1. When too many similar sigma points are used in the BUF, the resulting predicted measurement covariance matrix becomes poorly conditioned. Given an estimated state $\mathbf{x}_{\text{est}}$ of n_{est} variables, a total of $2n_{\text{est}} + 1$ sigma points is generated. Each one of them is then propagated to each of the n_{meas} time instant in t_{meas}. More measurements time instants per orbit means that the interval between them is reduced, thus increasing the likelihood that the measurements obtained from time-adjacent sigma points are very close to each other, making the columns of the covariance matrix close to linearly dependent. As a result, some eigenvalues shrink toward zero, making the matrix nearly singular and difficult to invert reliably. Since the inversion of $\mathbf{P}^{\mathbf{y}}$ is required in the computation of the Kalman-like gain, this numerical ill-conditioning leads to instability and large sensitivity to round-off errors. This issue is removed by substantially reducing the number of measurements given to the filter. Coincidentally, this also cuts the computation time by approximately two orders of magnitude: from ≈ 2.38 (s) to ≈ 0.03 (s).

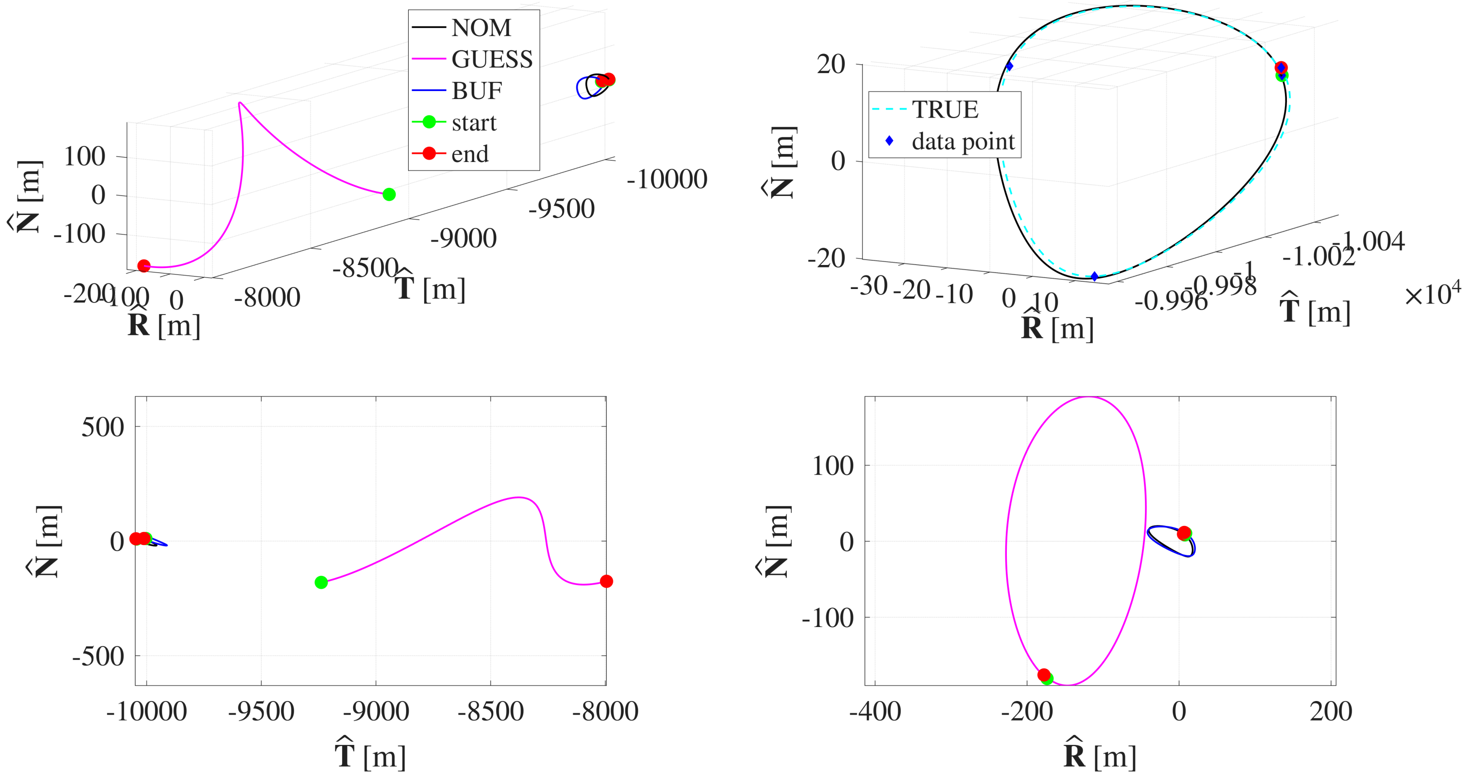

Fig. 3 **Analysis 2 (LEO1 - RO3): Results of the estimation procedure.**

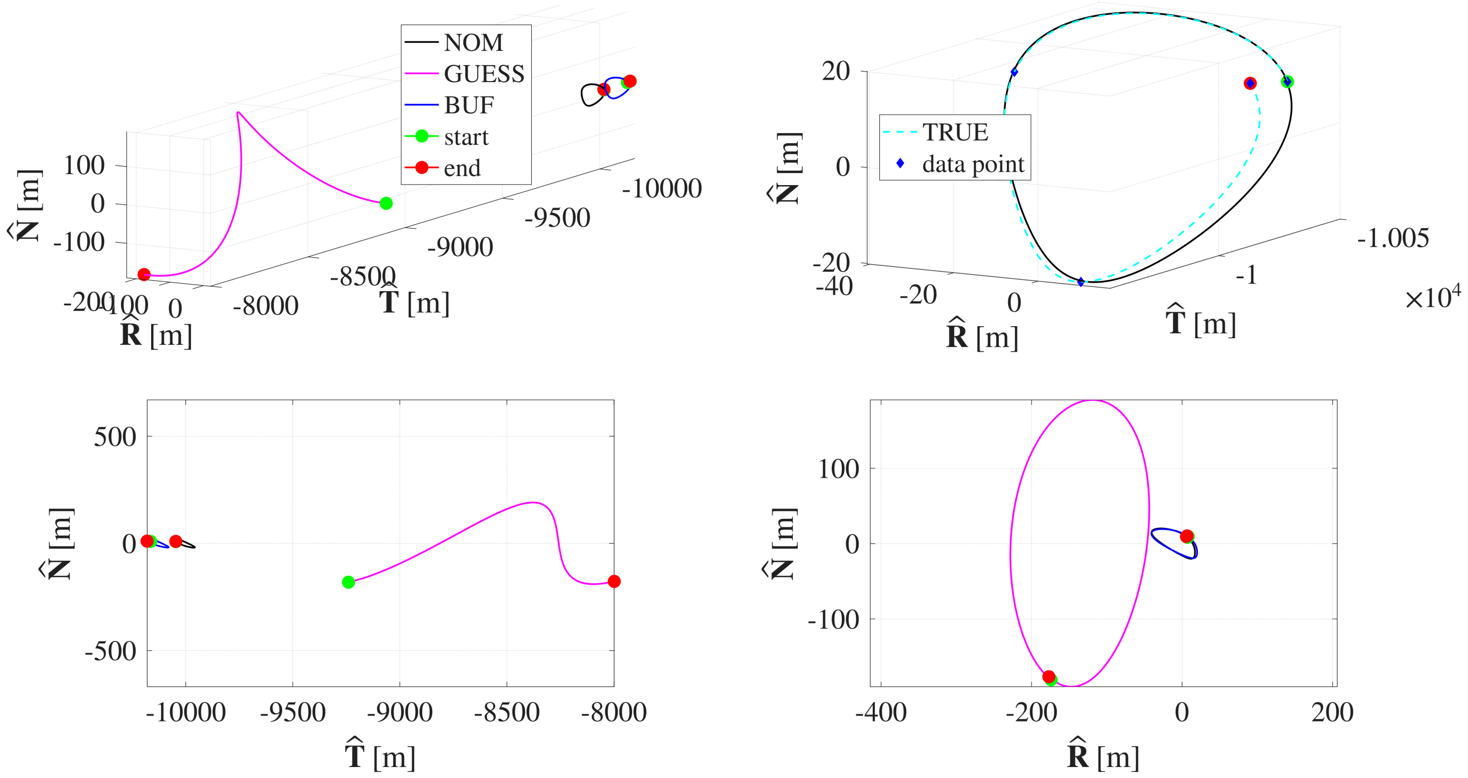

Fig. 4 **Analysis 2 (LEO2 - RO3): Results of the estimation procedure.**

5 Conclusions

This work presented a novel Batch Unscented Filter (BUF) for fast and accurate angles-only relative orbit determination (ROD), obtained by reformulating and extending the algorithm originally proposed by Park et al. [23]. The key modifications include the use of an analytical propagation model (replacing numerical integration), an augmented state vector, Monte Carlo-tuned UT parameters, and a UKF-inspired covariance update. Preliminary analyses in representative low-Earth orbit scenarios yielded the following key findings:

- The BUF consistently improves the accuracy of the initial guess, converging to reliable estimates even in the presence of strong perturbations such as differential drag (LEO2 scenarios) and under limited observability conditions (RO3 scenarios).
- In all cases, the filter reduced estimation errors to acceptable levels.
- A particularly surprising outcome was obtained in the second analysis, where reducing the amount of measurement data did not degrade performance. On the contrary, BUF achieved similar and sometimes superior accuracy at a fraction of the computational cost, especially in the challenging RO3 configurations. This effect was attributed to improved numerical conditioning of the covariance matrix when fewer, well-spaced measurements were employed.

Overall, the BUF exhibits strong potential for space-borne implementation, given its robustness, accuracy, and low data requirements. It could enable autonomous onboard ROD using only minimal measurements collected over a single orbit.

Several aspects warrant further investigation in future work. First, Monte Carlo simulations should be conducted to validate the filter performance across a wider range of initial conditions and noise levels. Second, direct quantitative comparisons against the non-linear batch LSQ filter are needed to rigorously benchmark the BUF. Third, the robustness to measurement outliers should be assessed, as erroneous data points may significantly influence batch estimation performance. Fourth, the current approach of enforcing positive definiteness by zeroing off-diagonal covariance terms discards potentially useful correlation information; alternative methods such as nearest symmetric positive-definite projection or regularisation should be explored. Fifth, while reducing the number of measurements improved numerical conditioning in this study, systematic criteria for measurement selection should be developed. Finally, alternative sigma-point formulations, such as spherical simplex, may be considered to reduce collinearity issues while simultaneously decreasing computational effort due to their reduced number of sigma points.

Appendix

		$\bar{\rho}_\alpha \pm \sigma(\rho_\alpha)$ [arcsec]	$\bar{\rho}_\epsilon \pm \sigma(\rho_\epsilon)$ [arcsec]
LEO1 - RO1	**GUESS**	-17 ± 1006	-806 ± 415
	BUF	0 ± 40	0 ± 41
	NOM	0 ± 40	-3 ± 41
LEO1 - RO2	**GUESS**	-20 ± 1025	-849 ± 412
	BUF	0 ± 40	0 ± 41
	NOM	0 ± 40	-3 ± 41
LEO1 - RO3	**GUESS**	-9 ± 3668	-3252 ± 1353
	BUF	0 ± 41	21 ± 106
	NOM	0 ± 40	-3 ± 41
LEO2 - RO1	**GUESS**	-19 ± 1007	-786 ± 424
	BUF	-2 ± 40	-8 ± 41
	NOM	-1 ± 40	12 ± 42
LEO2 - RO2	**GUESS**	-22 ± 1026	-828 ± 421
	BUF	-1 ± 40	-7 ± 41
	NOM	-1 ± 40	12 ± 42
LEO2 - RO3	**GUESS**	-12 ± 3670	-3199 ± 1368
	BUF	-1 ± 42	19 ± 129
	NOM	-1 ± 40	44 ± 53

Table 7 Analysis 1: Mean and standard deviation of α and ϵ residuals grouped by scenario.

		$\bar{\rho}_\alpha \pm \sigma(\rho_\alpha)$ [arcsec]	$\bar{\rho}_\epsilon \pm \sigma(\rho_\epsilon)$ [arcsec]
LEO1 - RO1	**GUESS**	-30 ± 994	-875 ± 385
	BUF	-3 ± 44	-8 ± 47
	NOM	-3 ± 37	-5 ± 37
LEO1 - RO2	**GUESS**	-32 ± 1003	-901 ± 381
	BUF	-3 ± 44	-8 ± 47
	NOM	-3 ± 37	-5 ± 37
LEO1 - RO3	**GUESS**	-55 ± 3393	-3091 ± 1246
	BUF	-3 ± 46	-12 ± 48
	NOM	-3 ± 37	-6 ± 38
LEO2 - RO1	**GUESS**	-28 ± 994	-864 ± 391
	BUF	-2 ± 38	-1 ± 38
	NOM	-3 ± 37	3 ± 38
LEO2 - RO2	**GUESS**	-30 ± 1004	-889 ± 387
	BUF	-2 ± 38	-1 ± 38
	NOM	-3 ± 37	3 ± 38
LEO2 - RO3	**GUESS**	-48 ± 3391	-3060 ± 1259
	BUF	-3 ± 40	-3 ± 37
	NOM	-3 ± 37	19 ± 42

Table 8 Analysis 2: Mean and standard deviation of α and ϵ residuals grouped by scenario.

		$e_{a\delta a} \pm \sigma(a\delta a)$ (m)	$e_{a\delta\lambda} \pm \sigma(a\delta\lambda)$ (m)	$e_{a\delta e_x} \pm \sigma(a\delta e_x)$ (m)	$e_{a\delta e_y} \pm \sigma(a\delta e_y)$ (m)	$e_{a\delta i_x} \pm \sigma(a\delta i_x)$ (m)	$e_{a\delta i_y} \pm \sigma(a\delta i_y)$ (m)	$e_{a_O} \pm \sigma(a_O)$ (m)
LEO1 - RO1	**GUESS**	−129.7 ± 100.0	917.4 ± 1000.0	17.7 ± 100.0	75.5 ± 100.0	−59.1 ± 100.0	184.4 ± 100.0	−538.2 ± 1000.0
	BUF	5.7 ± 3.0	826.4 ± 836.9	10.7 ± 11.4	3.6 ± 2.2	−10.6 ± 11.5	−3.3 ± 2.2	57.9 ± 60.2
LEO1 - RO2	**GUESS**	−129.7 ± 100.0	917.4 ± 1000.0	17.7 ± 100.0	75.5 ± 100.0	−59.1 ± 100.0	184.4 ± 100.0	−538.2 ± 1000.0
	BUF	7.0 ± 2.7	817.0 ± 927.5	10.7 ± 12.7	3.5 ± 2.2	−10.4 ± 12.7	−3.2 ± 2.1	59.4 ± 60.3
LEO1 - RO3	**GUESS**	−129.7 ± 100.0	917.4 ± 1000.0	17.7 ± 100.0	75.5 ± 100.0	−59.1 ± 100.0	184.4 ± 100.0	−538.2 ± 1000.0
	BUF	16.1 ± 0.3	−1886.6 ± 80.2	−4.9 ± 0.3	4.0 ± 0.4	4.3 ± 0.4	−1.8 ± 0.4	695.7 ± 16.0
LEO2 - RO1	**GUESS**	−129.7 ± 100.0	917.4 ± 1000.0	17.7 ± 100.0	75.5 ± 100.0	−59.1 ± 100.0	184.4 ± 100.0	−538.2 ± 1000.0
	BUF	1.9 ± 2.2	877.0 ± 483.0	12.7 ± 6.7	0.3 ± 1.8	−9.7 ± 6.8	−3.0 ± 1.8	39.3 ± 43.7
LEO2 - RO2	**GUESS**	−129.7 ± 100.0	917.4 ± 1000.0	17.7 ± 100.0	75.5 ± 100.0	−59.1 ± 100.0	184.4 ± 100.0	−538.2 ± 1000.0
	BUF	3.4 ± 2.0	897.2 ± 546.7	13.0 ± 7.6	0.2 ± 1.8	−10.0 ± 7.6	−2.9 ± 1.7	42.9 ± 42.9
LEO2 - RO3	**GUESS**	−129.7 ± 100.0	917.4 ± 1000.0	17.7 ± 100.0	75.5 ± 100.0	−59.1 ± 100.0	184.4 ± 100.0	−538.2 ± 1000.0
	BUF	20.4 ± 0.3	−2714.6 ± 75.6	−6.5 ± 0.3	3.1 ± 0.4	6.9 ± 0.4	−1.9 ± 0.4	959.9 ± 15.3

Table 9 Analysis 1: Estimation error components of GUESS and BUF values grouped by scenario.

		$e_{a\delta a} \pm \sigma(a\delta a)$ (m)	$e_{a\delta\lambda} \pm \sigma(a\delta\lambda)$ (m)	$e_{a\delta e_x} \pm \sigma(a\delta e_x)$ (m)	$e_{a\delta e_y} \pm \sigma(a\delta e_y)$ (m)	$e_{a\delta i_x} \pm \sigma(a\delta i_x)$ (m)	$e_{a\delta i_y} \pm \sigma(a\delta i_y)$ (m)	$e_{a_O} \pm \sigma(a_O)$ (m)
LEO1 - RO1	**GUESS**	−129.7 ± 100.0	917.4 ± 1000.0	17.7 ± 100.0	75.5 ± 100.0	−59.2 ± 100.0	184.4 ± 100.0	−538.2 ± 1000.0
	BUF	3.0 ± 7.6	868.4 ± 1081.1	6.4 ± 16.2	4.4 ± 7.7	−12.6 ± 15.9	−7.7 ± 7.8	7.3 ± 313.7
LEO1 - RO2	**GUESS**	−129.7 ± 100.0	917.4 ± 1000.0	17.7 ± 100.0	75.5 ± 100.0	−59.2 ± 100.0	184.4 ± 100.0	−538.2 ± 1000.0
	BUF	4.5 ± 7.7	849.2 ± 1104.3	6.2 ± 16.3	4.4 ± 7.6	−12.3 ± 16.2	−7.6 ± 7.8	9.7 ± 319.7
LEO1 - RO3	**GUESS**	−129.7 ± 100.0	917.4 ± 1000.0	17.7 ± 100.0	75.5 ± 100.0	−59.2 ± 100.0	184.4 ± 100.0	−538.2 ± 1000.0
	BUF	0.7 ± 2.1	45.3 ± 968.8	−1.5 ± 2.6	1.1 ± 2.2	−0.6 ± 2.6	−2.8 ± 2.0	−108.6 ± 242.9
LEO2 - RO1	**GUESS**	−129.7 ± 100.0	917.4 ± 1000.0	17.7 ± 100.0	75.5 ± 100.0	−59.2 ± 100.0	184.4 ± 100.0	−538.2 ± 1000.0
	BUF	6.8 ± 7.6	859.8 ± 1080.9	10.2 ± 16.1	5.4 ± 7.8	−12.8 ± 15.9	−3.6 ± 7.8	190.9 ± 301.5
LEO2 - RO2	**GUESS**	−129.7 ± 100.0	917.4 ± 1000.0	17.7 ± 100.0	75.5 ± 100.0	−59.2 ± 100.0	184.4 ± 100.0	−538.2 ± 1000.0
	BUF	8.3 ± 7.7	835.9 ± 1108.4	10.0 ± 16.3	5.3 ± 7.7	−12.5 ± 16.2	−3.5 ± 7.8	196.1 ± 306.9
LEO2 - RO3	**GUESS**	−129.7 ± 100.0	917.4 ± 1000.0	17.7 ± 100.0	75.5 ± 100.0	−59.2 ± 100.0	184.4 ± 100.0	−538.2 ± 1000.0
	BUF	1.6 ± 3.6	−114.9 ± 1584.1	−0.3 ± 4.0	0.9 ± 3.1	−0.7 ± 4.0	−1.7 ± 3.0	115.5 ± 372.5

Table 10 Analysis 2: Estimation error components of GUESS and BUF values grouped by scenario.

Acknowledgments

This research is funded by Infinite Orbits SAS, grant reference:
UA.A.RRR.DAER.ELABS.AUTO.G8E4RICC00 PhD-GNC Rendezvous - RIF. 10/2024 GAIAS.
The Authors would like to acknowledge GNC Engineer Daniel Opoka and GNC Engineer Raffaele Tarone for their support.

Declaration of Use of Artificial Intelligence

AI support was limited to acceptable purposes under the CEAS EuroGNC AI policy:

- Code development assistance: use of ChatGPT (GPT-5, 2025) in substitution of MATLAB documentation. In particular to search for built-in functions and generate examples for it. Help in implementation of trivial functions (*e.g.*, plots and tables). Help in formatting the code documentation. No impact is expected on the project as all the core algorithms are written by the authors. The very few and simple functions implemented by the AI were always double checked and tested.
- Proofreading and translation: use of ChatGPT (GPT-5, 2025) for grammar and style checks and synonyms suggestion to improve readability and language correctness. Help in translating from native language. Help in LaTeX commands.

References

[1] S. D'Amico. *Autonomous Formation Flying in Low Earth Orbit*. PhD thesis, Delft University of Technology, 2010. `https://elib.dlr.de/63481/1/Damico_PhD_01022010.pdf`.

[2] S. D'Amico, J.-S. Ardaens, and R. Larsson. Spaceborne autonomous formation-flying experiment on the prisma mission. *Journal of Guidance, Control, and Dynamics*, 35(3):834–850, 2012. doi: 10.2514/1.55638.

[3] C. Weeden, C. Blackerby, N. Okada, E. Yamamoto, J. Forshaw, and J. Auburn. Industry implementation of the long-term sustainability guidelines: An astroscale perspective. In *70th International Astronautical Congress (IAC)*, 2019.

[4] A. Scalvini, A. Suarez, S. R. Nekoo, and A. Ollero. Finite-time state-dependent riccati equation regulation of anthropomorphic dual-arm space manipulator system in free-flying conditions. *Acta Astronautica*, 216:504–517, 2024. doi: 10.1016/j.actaastro.2024.01.027.

[5] A. Scalvini, A. Fois, A. Suarez, S. R. Nekoo, and A. Ollero. Adaptive state-dependent riccati equation attitude control for rotation-flying dual-arm manipulators. In *Proceedings of the 2024 International Conference on Space Robotics (iSpaRo)*, pages 372–379, Luxembourg, 2024. IEEE. ISBN: 979-8-3503-6724-9. `https://ieeexplore.ieee.org/abstract/document/10687494`.

[6] S. Woicke, J. Jipp, C. Steimle, N. Pokrupa, and L. Metrailler. Adrios clearspace-1: In orbit demonstration of the removal of a non-cooperative spacecraft. In *Proceedings of the 9th European Conference on Space Debris*, volume 9. ESA Space Debris Office, 2025. `https://conference.sdo.esoc.esa.int/proceedings/sdc9/paper/317`.

[7] R. Biesbroek, S. Aziz, A. Wolahan, S. Cipolla, M. Richard-Noca, and L. Piguet. The clearspace-1 mission: Esa and clearspace team up to remove debris. In *Proceedings of the 8th European Conference on Space Debris*, volume 8, pages 1–3. ESA Space Debris Office, 2021. `https://conference.sdo.esoc.esa.int/proceedings/sdc8/paper/320`.

[8] D. C. Woffinden and D.-K. Geller. Observability criteria for angles-only navigation. *IEEE Transactions on Aerospace and Electronic Systems*, 45(3):1194–1208, 2009. doi: 10.1109/TAES.2009.5259193.

[9] T.A. Lovell and T. Lee. Numerical observability for relative satellite orbits with angles-only measurements. In *Proceedings of the 24th International Symposium on Space Flight Dynamics*, 2014. `https://issfd.org/ISSFD_2014/ISSFD24_Paper_S16-3_Lovell.pdf`.

[10] G. Gaias and J.-S. Ardaens. Flight demonstration of autonomous noncooperative rendezvous in low earth orbit. *Journal of Guidance, Control, and Dynamics*, 41(6):1337–1354, 2018. doi: 10.2514/1.G003239.

[11] G. Di Mauro, M. Lawn, and R. Bevilacqua. Survey on guidance navigation and control requirements for spacecraft formation-flying missions. *Journal of Guidance, Control, and Dynamics*, 41(3):581–602, 2018. ISSN: 0731-5090. doi: 10.2514/1.G002868.

[12] J.-S. Ardaens and G. Gaias. Flight demonstration of spaceborne real-time angles-only navigation to a noncooperative target in low earth orbit. *Acta Astronautica*, 153:367–382, 2018. doi: 10.1016/j.actaastro.2018.01.044.

[13] J. A. Sullivan. *Nonlinear Angles-Only Orbit Estimation for Autonomous Distributed Space Systems*. PhD thesis, Stanford University, 2020. `https://purl.stanford.edu/yx801sv8482`.

[14] J. Sullivan and S. D'Amico. Adaptive filtering for maneuver-free angles-only navigation in eccentric orbits. In *Proceedings of the 27th AAS/AIAA Space Flight Mechanics Meeting*, 2017. `https://slab.sites.stanford.edu/sites/g/files/sbiybj25201/files/media/file/sfm2017_sullivandamico.pdf`.

[15] J. Kruger, S. S. Hwang, and S. D'Amico. Starling formation-flying optical experiment: Initial operations and flight results, 2024. `https://arxiv.org/abs/2406.06748`.

[16] J.Kruger. *Flight Algorithms for Autonomous Tracking And Navigation of Distributed Space Systems Using Inter-Satellite Bearing Angles*. PhD thesis, Stanford University, 2024. `https://justin.zone/thesis_kruger_final_online.pdf`.

[17] J.-S. Ardaens. *Angles-Only Relative Navigation in Low Earth Orbit*. PhD thesis, Delft University of Technology, 2020. `https://pure.tudelft.nl/ws/portalfiles/portal/82719048/dissertation.pdf`.

[18] O. Montenbruck and E. Gill. *Satellite Orbits: Models, Methods, and Applications*. Springer-Verlag, 1st edition, 2000. ISBN: 978-3-540-67280-7.

[19] G. Gaias, S. D'Amico, and J.-S. Ardaens. Angles-only navigation to a noncooperative satellite using relative orbital elements. *Journal of Guidance, Control, and Dynamics*, 37(2):439–451, 2014. doi: 10.2514/1.61494.

[20] S. D'Amico, J.-S. Ardaens, G. Gaias, H. Benninghoff, B. Schlepp, and J. L. Jørgensen. Noncooperative rendezvous using angles-only optical navigation: System design and flight results. *Journal of Guidance, Control, and Dynamics*, 36(6):1576–1595, 2013. doi: 10.2514/1.59236.

[21] J.-S. Ardaens and G. Gaias. Angles-only relative orbit determination in low earth orbit. *Advances in Space Research*, 61(11):2740–2760, 2018. doi: 10.1016/j.asr.2018.03.016.

[22] A. Scalvini, G. Borelli, and G. Gaias. Towards robust angles-only relative orbit navigation: Assessing key modelling factors using batch least squares filtering. In *Proceedings of the 11th European Conference for Aeronautics and Aerospace Sciences (EUCASS)*, 2025.

[23] E. S. Park, S. Y. Park, K. M. Roh, and K. H. Choi. Satellite orbit determination using a batch filter based on the unscented transformation. *Aerospace Science and Technology*, 14(6):387–396, 2010. doi: 10.1016/j.ast.2010.03.007.

[24] G. Gaias, C. Colombo, and M. Lara. Analytical framework for precise relative motion in low earth orbits. *Journal of Guidance, Control, and Dynamics*, 43(5):915–927, 2020. doi: 10.2514/1.G004716.

[25] G. Gaias, J.-S. Ardaens, and C. Colombo. Precise line-of-sight modelling for angles-only relative navigation. *Advances in Space Research*, 67(11):3515–3526, 2021. doi: 10.1016/j.asr.2020.05.048.

[26] A. W. Koenig and S. D'Amico. Observability-aware numerical algorithm for angles-only initial relative orbit determination. In *Proceedings of the AAS/AIAA Astrodynamics Specialist Conference*, 2020. `https://slab.sites.stanford.edu/sites/g/files/sbiybj25201/files/media/file/bod_aas_2020_final.pdf`.

[27] A. W. Koenig, T. Guffanti, and S. D'Amico. New state transition matrices for spacecraft relative motion in perturbed orbits. *Journal of Guidance, Control, and Dynamics*, 40(7):1749–1768, 2017. doi: 10.2514/1.G002409.